

Many-body levels of optically excited and multiply charged InAs nanocrystals modeled by semiempirical tight binding

Seungwon Lee,^{1,2} Jeongnim Kim,² Lars Jönsson,² and John W. Wilkins¹¹*Department of Physics, Ohio State University, Columbus, Ohio 43210*²*National Center for Supercomputing Applications, University of Illinois at Urbana-Champaign, Urbana, Illinois 61801*

Garnett W. Bryant

National Institute of Standards and Technology, Gaithersburg, Maryland 20899

Gerhard Klimeck

Jet Propulsion Laboratory, California Institute of Technology, Pasadena, California 91109

(Received 05 August 2002; revised manuscript received 27 September 2002; published 5 December 2002)

Many-body levels of optically excited and multiply charged InAs nanocrystals are studied with the semiempirical tight-binding model. Single-particle levels of unstrained spherical InAs nanocrystals are described by the $sp^3d^5s^*$ nearest-neighbor tight-binding model including spin-orbit coupling. For optically excited InAs nanocrystals, first-order corrections of electron-hole Coulomb and exchange interaction to exciton levels and the oscillator strengths of the exciton levels determine several low-lying, bright-exciton levels. The origin of the large oscillator strengths of the bright exciton levels is explained by the analysis of dominant angular momenta of exciton envelope functions. Good agreement with photoluminescence excitation experiments is achieved for the size dependence of the three lowest bright-exciton energies of InAs nanocrystals with radius larger than 20 Å. For multiply charged InAs nanocrystals, polarization of the nanocrystal environment is approximated by modeling the environment with a uniform dielectric medium. This polarization model incorporated into the tight-binding model provides a reasonable description of electron and hole addition energies in scanning tunneling spectroscopy experiments.

DOI: 10.1103/PhysRevB.66.235307

PACS number(s): 73.22.-f, 78.67.-n

I. INTRODUCTION

Recent advances in semiconductor quantum dot fabrications have opened up a rich opportunity to study zero-dimensional quantum systems of various sizes, shapes, and materials.¹⁻⁴ Quantum confinement and enhanced many-body interactions in the quantum dots lead to optical and transport properties that are dramatically different from those of higher dimensional and bigger systems.³⁻⁶ To utilize the unique properties, many applications such as low-threshold lasers, single-electron devices, memories, detectors, single photon emitters, and quantum information devices have been proposed and are being developed.⁷⁻¹² Hence the accurate modeling of the quantum confinement and many-body interactions is not only of fundamental interest, but is also important to help tailor quantum dots for a specific application.

Various theoretical approaches are used to study the quantum dots, ranging from first-principle calculations to empirical models.¹³⁻²³ Due to the generally high computational demand of the first-principle calculations, empirical models are widely employed to study quantum dots containing more than a few hundreds of atoms. The three empirical models primarily used are the multiband effective-mass approximation,¹⁶ the pseudopotential model,^{18,19} and the tight-binding model.²⁰⁻²³ The effective-mass approximation treats a quantum dot as a confined bulk and continuum system, while the pseudopotential and tight-binding models treat as an extended molecular system with the atomistic description of ionic potentials. The distinction between the two atomistic models lies in the degree of atomic detail included in the

model. Within the tight-binding model, the atomistic detail is limited to a small basis set, while in the pseudopotential model a detailed local variation of wave functions is described with a large basis set. Therefore the tight-binding model is computationally less costly than the pseudopotential model. The tight-binding model is a good candidate for the study of relatively big, complicated systems where both the computational efficiency and atomistic description are required. An example of such a system is vertically stacked, self-assembled quantum dots which contain not only millions of atoms but also a thin barrier and sharp edges and points.²⁴ Because of the computational efficiency of this atomistic model, we choose the tight-binding model to study quantum dots.

Modeling chemically synthesized nanocrystals is a good starting point to test the applicability of the tight-binding model to quantum dots. The nanocrystals are unstrained and spherical.³ The nanocrystal sizes can be tuned by changing chemical-synthesis conditions.²⁵ The easy control of the nanocrystal size enables the study of size-dependent properties without involving such complexities as strains and shapes. In this work, we examine the accuracy of the tight-binding model in describing the optical and transport properties of nanocrystals with a wide range of sizes.

Recently, two complementary experiments have provided a picture of the many-body levels of InAs nanocrystals.^{26,27} First, photoluminescence excitation (PLE) experiments examined exciton levels by optically creating electron-hole pairs.²⁶ Second, scanning tunneling microscope (STM) experiments probed individual electron (hole) levels by con-

secutively charging the nanocrystal with one electron (hole) at a time.²⁷ The exciton creation and the electron (hole) addition experiments probe single-particle energies and many-body interactions of the nanocrystals. The many-body interaction involved in the exciton creation is an electron-hole interaction, while that in the electron and hole addition is an extra-charge-carrier interaction within the polarization of the nanocrystal and its environment. Furthermore, the exciton creation is an optically selective process. In spherical nanocrystals, the optical selection rules are determined by almost exact conservation of angular momentum.

The many-body levels probed by the PLE and STM experiments have been theoretically investigated with various empirical models. An extended effective-mass theory to include the coupling between conduction and valence bands improved the description of the exciton levels of narrow-gap InAs nanocrystals.²⁶ Pseudopotential studies clarified the difference between exciton gaps and quasiparticle gaps, which can be measured by the PLE and STM experiments, respectively.^{18,19} The studies also demonstrated that the exciton gaps are much less sensitive to a dielectric mismatch at the nanocrystal surface than the quasiparticle gaps.^{19,28} Tight-binding studies of exciton gaps showed that the model with an sp^3s^* basis set underestimates exciton gaps by a few hundreds of meV,²³ but the inclusion of d orbitals and spin-orbit coupling improves the gaps by raising the gaps by as much as 0.2 eV.²¹ However, exciton levels above the gaps and their oscillator strengths have not been investigated in the previous tight-binding studies.^{23,21}

In this paper, we study the many-body levels of optically excited and multiply charged InAs nanocrystals in the framework of the empirical tight-binding model. We employ the $sp^3d^5s^*$ nearest-neighbor tight-binding model including spin-orbit coupling to describe single-particle levels. We incorporate electron-hole interactions and dipole transitions into the tight-binding model to investigate the exciton levels of the optically excited nanocrystals. Several low-lying, bright-exciton levels are identified by their large oscillator strengths. The analysis of the angular momentum of the exciton envelope functions reveals the origin of the large oscillator strengths. The electron and hole addition energies of the multiply charged nanocrystals are described with the sum of single-particle energies and charging energies. The present model includes three types of charging energies: (i) self-polarization energies, (ii) charge-carrier Coulomb energies, and (iii) electron-removal work functions. The remainder of the paper is structured as follows. Section II describes the models for absorption spectra and electron and hole addition energies. Section III presents results. Section IV provides discussions about the results.

II. MODEL

One key element in modeling the many-body levels of optically excited and multiply charged nanocrystals is the single-particle levels. In this work, the single-particle levels are calculated with the $sp^3d^5s^*$ nearest-neighbor tight-binding model including spin-orbit coupling. The nanocrystal is modeled as an unstrained, spherical, and anion-atom

centered zinc-blende crystallite. To mimic the surface passivation by ligands,²⁷ the energies of dangling bonds at the surface are shifted well above the band gap of bulk InAs. We use tight-binding parameters of Jancu *et al.*²⁹ The parameters give a good description of the effective masses of the lowest conduction, heavy-, light-hole, and spin-split bands near Γ point and the band energies at the high-symmetry points.²⁹ A recent tight-binding study on GaAs/AlAs superlattices shows that the parameters of Jancu *et al.* for GaAs and AlAs produce incorrect effective masses of the lowest conduction band near the X point, yielding incorrect optoelectrical properties of the superlattice.³⁰ However, this problem, if exists in the InAs parameters, should have very little impact on the low-lying single-particle energies of nanocrystals since the energies are mainly determined by the band structure near the Γ point. The Appendix gives a brief description of the construction of the single-particle Hamiltonian and the calculation of the single-particle levels.

Single-particle levels above a Fermi energy somewhere within the band gap are electron levels, whereas levels below the Fermi energy are related to hole levels.³¹ The electron states $|e\rangle$ with energy E^e and the hole states $|h\rangle$ with energy E^h are linear combinations of tight-binding basis orbitals $|i\gamma\sigma\rangle$:

$$|e\rangle = \sum_{i\gamma\sigma} c_{e;i\gamma\sigma} |i\gamma\sigma\rangle, \quad (1)$$

$$|h\rangle = \sum_{i\gamma\sigma} c_{h;i\gamma\sigma} |i\gamma\sigma\rangle, \quad (2)$$

where tight-binding indices i , γ , and σ denote an atom site, orbital type, and spin, respectively. The coefficients $c_{e;i\gamma\sigma}$ and $c_{h;i\gamma\sigma}$ describe a variation of a single-particle state from one atomic site to another atomic site, while the basis orbital $|i\gamma\sigma\rangle$ describes a local variation of the state near one atomic site. The global variation described by the coefficient $c_{i\gamma\sigma}$ is called an envelope function of the γ -basis orbital.

Many-body interactions are incorporated into the tight-binding model as perturbations to the single-particle Hamiltonian. The many-body interactions are electron-hole Coulomb and exchange interactions in the optically excited nanocrystals, and charge-carrier interactions and the polarization of the environment in the multiply charged nanocrystals. It is a reasonable approximation to treat the many-body interactions as perturbations because their contributions to the many-body energies are typically one order of magnitude smaller than those of the single-particle energies. The modeling of the many-body interactions requires a real-space description of the tight-binding basis orbitals. We use Slater orbitals to describe the basis orbitals. In our previous work, we show that this representation is reliable for the study of relatively large nanocrystals.²³ The Slater orbitals for In and As atoms are listed in Table I.

A. Exciton absorption spectra

To model the exciton levels of optically excited nanocrystals, we first define exciton states and energies. Exciton states

TABLE I. Slater orbitals of In and As atoms. In Slater orbitals, the radial part of the wave function is written as $R(r) = r^a \exp(-br)$, where the constant a and b are determined by the Slater rules (Ref. 43). The angular part of the Slater orbital is given by the spherical harmonics Y_{lm} .

Orbital	In	As
s	$0.31 r^3 e^{-1.25r} Y_{00}$	$1.61 r^{2.7} e^{-1.7r} Y_{00}$
p	$0.31 r^3 e^{-1.25r} Y_{1m}$	$1.61 r^{2.7} e^{-1.7r} Y_{1m}$
d	$0.00022 r^3 e^{-0.25r} Y_{2m}$	$0.0007 r^{2.7} e^{-0.27r} Y_{2m}$
s^*	$0.00034 r^{3.2} e^{-0.31r} Y_{00}$	$0.0018 r^3 e^{0.4r} Y_{00}$

are defined as a product of the electron and hole states. The projection of the exciton state $|eh\rangle$ into electron (e) and hole (h) spatial (\mathbf{r}) and spin (σ) spaces is

$$\langle \mathbf{r}_e, \sigma_e; \mathbf{r}_h, \sigma_h | eh \rangle = \psi_e(\mathbf{r}_e, \sigma_e) \psi_h(\mathbf{r}_h, \sigma_h). \quad (3)$$

Exciton energies are defined as the sum of the electron and hole energies and the first-order corrections of the electron-hole Coulomb J and exchange K interactions:

$$E_{eh} = E^e + E^h + \langle eh | J | eh \rangle + \langle eh | K | eh \rangle. \quad (4)$$

The Coulomb and exchange interactions are screened by dielectric function $\epsilon(|\mathbf{r} - \mathbf{r}'|, R)$ which is a function of the separation $|\mathbf{r} - \mathbf{r}'|$ of two particles, and nanocrystal radius R .²³ For short-range Coulomb and exchange interactions, the separation dependence of the dielectric function is approximated by the Thomas-Fermi model of Resta.³² For long-range interactions, the radius dependence of the dielectric function is determined by the Penn model generalized for quantum dots.^{33,34} The first-order corrections of the Coulomb J and exchange K interactions screened by the dielectric function are

$$\langle eh | J | eh \rangle = -e^2 \sum_{\sigma\sigma'} \int \int d^3r' d^3r \times \frac{\psi_e^*(\mathbf{r}, \sigma) \psi_e(\mathbf{r}, \sigma) \psi_h^*(\mathbf{r}', \sigma') \psi_h(\mathbf{r}', \sigma')}{\epsilon(|\mathbf{r} - \mathbf{r}'|, R) |\mathbf{r} - \mathbf{r}'|}, \quad (5)$$

$$\langle eh | K | eh \rangle = e^2 \sum_{\sigma\sigma'} \int \int d^3r' d^3r \times \frac{\psi_e^*(\mathbf{r}, \sigma) \psi_h^*(\mathbf{r}, -\sigma) \psi_e(\mathbf{r}', \sigma') \psi_h(\mathbf{r}', -\sigma')}{\epsilon(|\mathbf{r} - \mathbf{r}'|, R) |\mathbf{r} - \mathbf{r}'|}. \quad (6)$$

Details about the dielectric function and the calculation of the Coulomb and exchange interaction matrix elements are described in our previous paper.²³

The oscillator strengths of exciton states are calculated to determine optically allowed states. The oscillator strength of the exciton state $|eh\rangle$ is defined as

$$S(E_{eh}) = \frac{2m_e}{\hbar} E_{eh} |\langle eh | \hat{\mathbf{r}} | 0 \rangle|^2, \quad (7)$$

where m_e is the free-electron mass. The matrix element $\langle eh | \hat{\mathbf{r}} | 0 \rangle$ is the dipole moment between initial state $|0\rangle$ with no electron-hole pair and final state $|eh\rangle$ with an electron-hole pair. The exciton absorption spectrum is given by

$$\sigma_{\text{abs}}(E) \sim \sum_{eh} S(E_{eh}) \delta(E - E_{eh}). \quad (8)$$

To mimic thermal broadening, exciton life times, nanocrystal size inhomogeneity, etc., the exciton absorption peaks are broadened with a Gaussian function:

$$\sigma_{\text{abs}}(E) \sim \sum_{eh} S(E_{eh}) \exp[-(E - E_{eh})^2 / \sigma^2], \quad (9)$$

where σ is the linewidth of the Gaussian function. The linewidth is chosen to be 10 meV to be comparable to the broadening (50 meV) of experimental photoluminescence spectra.²⁶

The dipole moment is naturally divided into two parts in the tight-binding model. A single-particle state in the tight-binding model is composed of two functions: (i) an envelope function describing the global variation of the state, and (ii) a basis orbital describing the local variation of the state. To match the composition of the state, the dipole moment operator $\hat{\mathbf{r}}$ is decomposed into a discrete position vector operator $\hat{\mathbf{r}}_i$ of atom site i and a relative position vector operator $\delta\hat{\mathbf{r}}_i = (\hat{\mathbf{r}} - \hat{\mathbf{r}}_i)$.²⁰ With this decomposition, the dipole moment matrix element becomes

$$\langle eh | \hat{\mathbf{r}} | 0 \rangle = \sum_{ii' \gamma\gamma' \sigma} c_{e;ii' \gamma' \sigma}^* c_{h;ii' \gamma - \sigma}^* [\mathbf{r}_i \delta_{ii'} \delta_{\gamma\gamma'} + \langle i' \gamma' | \delta\hat{\mathbf{r}}_i | i \gamma \rangle] \approx \sum_{i\gamma\gamma' \sigma} c_{e;i\gamma' \sigma}^* c_{h;i\gamma - \sigma}^* [\mathbf{r}_i \delta_{\gamma\gamma'} + \langle i\gamma' | \delta\hat{\mathbf{r}}_i | i\gamma \rangle]. \quad (10)$$

The second part of the dipole moment is approximated by including only the matrix elements between the basis orbitals on the same atom site. This approximation is reasonable since our calculation shows that the dipole moment from the neglected matrix elements is at least one order of magnitude smaller than that from the retained matrix elements. The first part of the dipole moment is the dipole moment between the envelope functions of the same orbital, while the second part is that between the envelope functions of different orbitals. From here on, we call the former an *intraorbital* dipole moment and the latter an *interorbital* dipole moment.

In both intra- and interorbital dipole moments, the total angular momentum difference ΔJ between electron and hole states should be unity. However, the rule $\Delta J = 1$ is satisfied differently. The decomposition of the dipole moment operator into $\hat{\mathbf{r}}_i$ and $\delta\hat{\mathbf{r}}_i$ leads to the decomposition of the total angular momentum operator \vec{J} into two operators; $\vec{J} = \vec{L} + \vec{j}$ where \vec{L} and \vec{j} are the global angular momentum operator of an envelope function and the local total angular momentum operator of a basis orbital, respectively. The operator \vec{j} is

TABLE II. Nonzero local dipole moments between tight-binding basis orbitals for In and As with a dipole operator in z direction. The dipole moments are calculated by representing the orbitals in real space with Slater orbitals (Ref. 43), and by using a numerical integration with the Simpson's rule (Ref. 35) for the radial parts and an exact integration for the angular parts.

Dipole moment	In (Å)	As (Å)
$\langle s \delta \hat{z} p_z \rangle$	1.106	0.754
$\langle s^* \delta \hat{z} p_z \rangle$	0.196	0.123
$\langle p_z \delta \hat{z} d_{3z^2-r^2} \rangle$	0.116	0.049
$\langle p_x \delta \hat{z} d_{zx} \rangle$	0.101	0.043
$\langle p_y \delta \hat{z} d_{yz} \rangle$	0.101	0.043

further given by $\vec{l} + \vec{s}$, where \vec{l} and \vec{s} are the angular momentum and spin operator of a basis orbital. With respect to the global L and local j angular momentum eigenvalues, the optical selection rules of the intra- and interorbital dipole moments are

$$\Delta L = 1 \text{ and } \Delta j = 0, \text{ for intraorbital,} \quad (11)$$

$$\Delta L = 0 \text{ and } \Delta j = 1, \text{ for interorbital.} \quad (12)$$

Local dipole moments $\langle i\gamma' | \delta \hat{r}_i | i\gamma \rangle$ between basis orbitals are evaluated for the intraorbital dipole moment. Table II lists the pairs of basis orbitals that have nonzero local dipole moments due to the selection rule $\Delta j = 1$. The dipole moments of those pairs are evaluated with a numerical integration with the Simpson's rule³⁵ for the radial part and an exact integration for the angular part. The calculated dipole moments are listed in Table II. An alternative way to determine the dipole moments is to fit them to bulk absorption spectra.²⁰

B. Electron and hole addition energies

Recently, the electron and hole addition energies of InAs nanocrystals were probed by STM experiments, where the tunneling current between an STM metallic tip and an InAs nanocrystal are measured as a function of the bias voltage applied between the tip and the nanocrystal.²⁷ Electron and hole addition energies manifest themselves in the conductance peaks of the tunneling spectra, because each peak indicates that the Fermi energy of the tip is resonant with an addition energy. Figure 1 presents a schematic description of the conductance spectra and the STM experimental setup.

The addition energies consist of (i) single-particle energies of a nanocrystal and (ii) charging energies for single-electron transfer between a nanocrystal and a metal lead. Within the capacitor model, a charging energy for adding an electron or a hole in a system is e^2/C_{eff} where C_{eff} is an effective capacitance of the system. The capacitance C_{eff} depends on the geometry and dielectric constant of the system, but does not depend on the number of charges nor on the charge distributions in the system. The capacitor model sufficiently describes charging energies when the polarization of a system is a dominant source of the charging energy, and

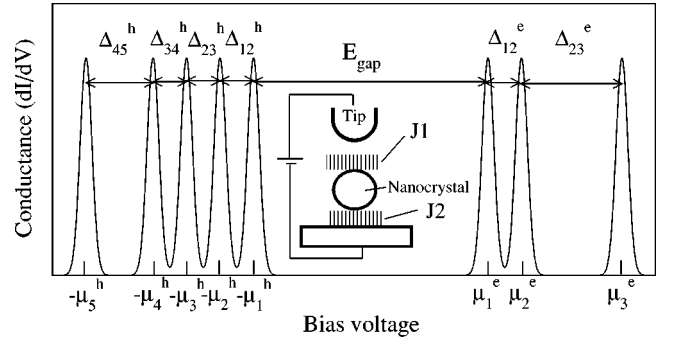


FIG. 1. Schematic description of the differential conductances of tunneling currents with respect to a bias voltage. Important physical quantities in the spectrum are labeled according to the definitions made in the paper. The inset is a schematic drawing of a double-barrier tunneling-junction configuration in STM tunneling measurements.

Coulomb interactions between charge carriers are negligible. However, as system sizes become as small as those of nanocrystals, strong quantum confinement enhances the Coulomb interactions. Furthermore, both the polarization and Coulomb energies are sensitive to charge distributions in strongly confined systems. Due to the limits of the capacitor model, we use a different model which includes charge-carrier Coulomb energies and describes charging energies in terms of charge distributions.

The energy condition for an electron to tunnel from a metal lead to a nanocrystal charged with $(n-1)$ electrons is met when the Fermi level of the metal μ_F^M is resonant with an n th electron addition energy μ_n^e of the nanocrystal:

$$\mu_F^M = \mu_n^e. \quad (13)$$

The n th electron addition energy is,¹⁹ i.e.,

$$\mu_n^e = E_n^e + \sum_n^{\text{pol,e}} + \sum_{i=1}^{n-1} J_{i,n}^{\text{ee}}. \quad (14)$$

The first term E_n^e is the energy of the n th electron level of the nanocrystal. The last two terms account for charging energies due to the polarization of the nanocrystal environment and many-body interactions. The second term $\sum_n^{\text{pol,e}}$ denotes the self-polarization energy of the n th electron, which is caused by the interaction between one electron and polarized charges at surfaces induced by the electron. Note that a dielectric mismatch between the nanocrystal and its surrounding leads to nonzero net polarized charges at the surface. The third term $J_{i,n}^{\text{ee}}$ represents a Coulomb energy due to the interaction between the n th electron and an electron in the nanocrystal. The Coulomb energy $J_{i,n}^{\text{ee}}$ has two components: a direct Coulomb energy $J_{i,n}^{\text{dir}}$ and a polarized Coulomb energy $J_{i,n}^{\text{pol}}$. The direct Coulomb energy results from a Coulomb interaction between two electrons in the absence of the dielectric mismatch at the surface. The polarized Coulomb energy is a correction to the Coulomb energy $J_{i,n}^{\text{ee}}$ due to the dielectric mismatch. The polarized Coulomb energy results from the interaction between one electron and the polarized

charges at the surface induced by another electron. Note that the exchange interaction between the n th electron and the other electrons in the nanocrystal is ignored in the present model since it is smaller than the experimental resolution (about 10 meV).²⁷

An electron can tunnel from a nanocrystal charged with $(n-1)$ holes to a metal lead when the Fermi energy of the metal lead matches the negative of an n th hole addition energy μ^h :

$$\mu_F^M = -\mu_n^h, \quad (15)$$

where the n th hole addition energy is

$$\mu_n^h = E_n^h + \sum_n^{\text{pol,h}} + \sum_{i=1}^{n-1} J_{i,n}^{\text{hh}} + W_n. \quad (16)$$

Removing an electron from the nanocrystal charged with $(n-1)$ holes can be seen as adding an n th hole to the nanocrystal. The n th hole level energy E_n^h is the negative of the energy of the valence electron removed from the nanocrystal. Similar to the counterparts in the electron addition energy, the charging energies $\sum_n^{\text{pol,h}}$ and $J_{i,n}^{\text{hh}}$ account for a hole self-polarization energy and a hole-hole Coulomb energy, respectively.

The last term in Eq. (16) represents a work required to remove an electron from the nanocrystal and add it to the metal lead in the presence of n holes in the nanocrystal. We call the last term an *electron-removal work function*. The electron-removal work function does not exist in the electron addition energies due to the screening effect of free electrons in the metal. When electrons tunnel from a metal lead to a nanocrystal and leave holes in the metal, the electric field generated by the holes is completely screened out by other free electrons in the metal. In other words, the tunneling electron does not see an attractive electric field generated by the holes in the metal. In contrast, when electrons tunnel from a nanocrystal to a metal lead, holes left in a nanocrystal are only partially screened by valence electrons in the nanocrystal. More importantly, the electron-removal work function is different from conventional work functions, which arise from charging distortions at surfaces. Although the conventional work function affects tunneling rates, it does not affect the energy condition of tunneling.

The absolute positions of the conductance peaks measured by STM experiments vary with respect to the Fermi energy of an unbiased STM tip, but spacings between the peaks remain the same. In the present model, the spacings are

$$\begin{aligned} \Delta_{n,n+1}^e &\equiv \mu_{n+1}^e - \mu_n^e = E_{n+1}^e - E_n^e + \sum_{n+1}^{\text{pol,e}} - \sum_n^{\text{pol,e}} \\ &+ \sum_{i=1}^n J_{i,n+1}^{\text{ee}} - \sum_{i=1}^{n-1} J_{i,n}^{\text{ee}}, \end{aligned} \quad (17)$$

$$\begin{aligned} \Delta_{n,n+1}^h &\equiv \mu_{n+1}^h - \mu_n^h = E_{n+1}^h - E_n^h + \sum_{n+1}^{\text{pol,h}} - \sum_n^{\text{pol,h}} \\ &+ \sum_{i=1}^n J_{i,n+1}^{\text{hh}} - \sum_{i=1}^{n-1} J_{i,n}^{\text{hh}} + W_1. \end{aligned} \quad (18)$$

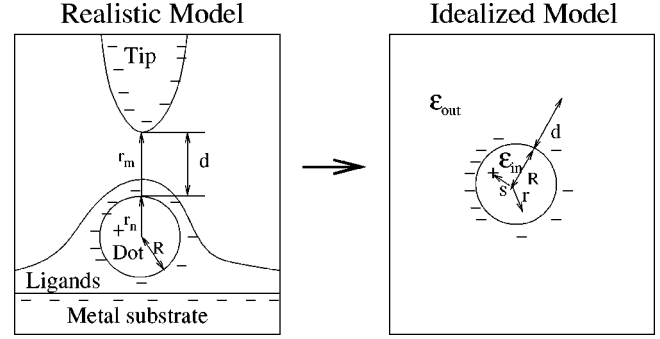


FIG. 2. Schematic diagram of the polarization of a charged nanocrystal and the environment in a realistic and an idealized model. In the realistic model, the polarization strongly depends on the geometry of the nanocrystal environment such as the shape of the STM tip and ligands, and distances between these components. In the idealized model, the inhomogeneous nanocrystal environment is replaced with a uniform dielectric medium characterized by an effective dielectric constant ϵ_{out} .

W_n is roughly n times larger than W_1 , assuming that the charge distribution of holes in the nanocrystal is almost spherically symmetric. Therefore the electron-removal work function difference $W_{n+1} - W_n$ is replaced with W_1 in $\Delta_{n,n+1}^h$.

The calculation of the charging energies requires a description of the electrostatic potential of a charged nanocrystal and the polarized environment. The potential is sensitive to the geometry of the nanocrystal and the environment. However, since details of the geometry in the STM experiment are unavailable²⁷ we approximate the nanocrystal environment with an infinite uniform dielectric medium.^{19,36} This idealized model captures the effects of a dielectric mismatch at the nanocrystal surfaces on the charging energies.¹⁹ Figure 2 presents a schematic diagram of the polarization of a charged nanocrystal and the environment within a realistic model and an idealized model.

When a nanocrystal is embedded in an infinite dielectric medium with dielectric constant ϵ_{out} , an electrostatic potential generated by an elementary charge e at point s inside the nanocrystal with dielectric constant ϵ_{in} and radius R is

$$\begin{aligned} V(\mathbf{r};\mathbf{s}) &= V^{\text{dir}}(\mathbf{r};s) + V^{\text{pol}}(\mathbf{r};s) \\ &= e \left[\frac{1}{\epsilon_{\text{in}}|\mathbf{r}-\mathbf{s}|} + \frac{\epsilon_{\text{in}} - \epsilon_{\text{out}}}{\epsilon_{\text{in}}R} \sum_{\ell=0}^{\infty} \left(\frac{r}{R} \right)^{\alpha_{\ell}} \right. \\ &\quad \left. \times \left(\frac{s}{R} \right)^{\ell} \frac{(\ell+1)P_{\ell}(\mathbf{r} \cdot \mathbf{s}/rs)}{\epsilon_{\text{out}} + \ell(\epsilon_{\text{in}} + \epsilon_{\text{out}})} \right], \end{aligned} \quad (19)$$

where α_{ℓ} is ℓ for r smaller than R , and $-\ell-1$ for r larger than R .³⁶ The function $P_{\ell}(x)$ is a ℓ th Legendre polynomial. The first term $V^{\text{dir}}(\mathbf{r};s)$ is a Coulomb potential of the source charge when there is no dielectric mismatch at the surface, while the second term $V^{\text{pol}}(\mathbf{r};s)$ results from the polarization of the dielectric medium outside the nanocrystal. In connection with the STM experimental setup²⁷ (see the inset of Fig.

1), $V^{\text{pol}}(\mathbf{r};\mathbf{s})$ is attributed to the polarization of the ligands, and the image charges of the STM tip and the metal substrate.

For the electrostatic potential $V(\mathbf{r};\mathbf{s})$, it is required to determine the dielectric constants of the nanocrystal and the environment. For $V^{\text{dir}}(\mathbf{r};\mathbf{s})$, we replace ϵ_{in} with $\epsilon(|\mathbf{r}-\mathbf{r}'|,R)$ to include the size and particle-separation dependence of the dielectric function (see Sec. II A). For $V^{\text{pol}}(\mathbf{r};\mathbf{s})$, we replace ϵ_{in} with $\epsilon(\infty,R)$ to treat the nanocrystal as a uniform dielectric medium. Note that $\epsilon(|\mathbf{r}-\mathbf{r}'|,R)$ saturates to $\epsilon(\infty,R)$ as $|\mathbf{r}-\mathbf{r}'|$ approaches to 2 Å. The dielectric constant ϵ_{out} is adjusted to fit $\Delta_{1,2}^c$ to the corresponding experimental value.

The three types of charging energies are calculated with charge densities given by the tight-binding wave function $\psi(\mathbf{r},\sigma)$ and with the electrostatic potential given by Eq. (19). First, the self-polarization energy results only from $V^{\text{pol}}(\mathbf{r};\mathbf{s})$ because the source charge does not interact with itself. The self-polarization energy of an i th tunneling electron or hole is written as

$$\Sigma_i^{\text{pol}} = \frac{e}{2} \sum_{\sigma} \int d^3r V^{\text{pol}}(\mathbf{r};\mathbf{s}) |\psi_i(\mathbf{r},\sigma)|^2, \quad (20)$$

where $\psi_i(\mathbf{r},\sigma)$ is the wave function of the i th electron or hole. Second, the Coulomb energy between a pair of electrons or holes is given by

$$J_{i,j} = e \sum_{\sigma\sigma'} \int d^3r_1 d^3r_2 V(\mathbf{r}_1;\mathbf{r}_2) |\psi_i(\mathbf{r}_1,\sigma)|^2 |\psi_j(\mathbf{r}_2,\sigma')|^2. \quad (21)$$

The Coulomb energy has two components: the direct Coulomb energy attributed to $V^{\text{dir}}(\mathbf{r};\mathbf{s})$ and the polarized Coulomb energy to $V^{\text{pol}}(\mathbf{r};\mathbf{s})$. Finally, the electron-removal work function is approximated as

$$W_1 = -e \sum_{\sigma} \int d^3r [V(\mathbf{r}_M;\mathbf{r}) - V(\mathbf{r}_N;\mathbf{r})] |\psi_1^h(\mathbf{r},\sigma)|^2 \\ \approx \frac{e^2}{\epsilon_{\text{out}}} \left[\frac{1}{R} - \frac{1}{R+d} \right], \quad (22)$$

where \mathbf{r}_M and \mathbf{r}_N are the position vector of the closest outer surface of the metal lead to the nanocrystal and that of the nanocrystal to the metal lead, respectively (see Fig. 2). The final equation is obtained by approximating the charge density of a hole with that of a point charge e at the nanocrystal center and by ignoring higher-order terms $\ell > 0$ of $V^{\text{pol}}(\mathbf{r};\mathbf{s})$. The symbol d is the closest distance between the nanocrystal and the metal lead as shown in Fig. 2.

III. RESULTS

A. Exciton absorption spectra

Figure 3 presents calculated exciton absorption spectra of InAs nanocrystals with various radii. As the radius increases, exciton energies decrease and their energy spacings become smaller. However, the absorption rate of each exciton level remains relatively unchanged. The lowest exciton level D1

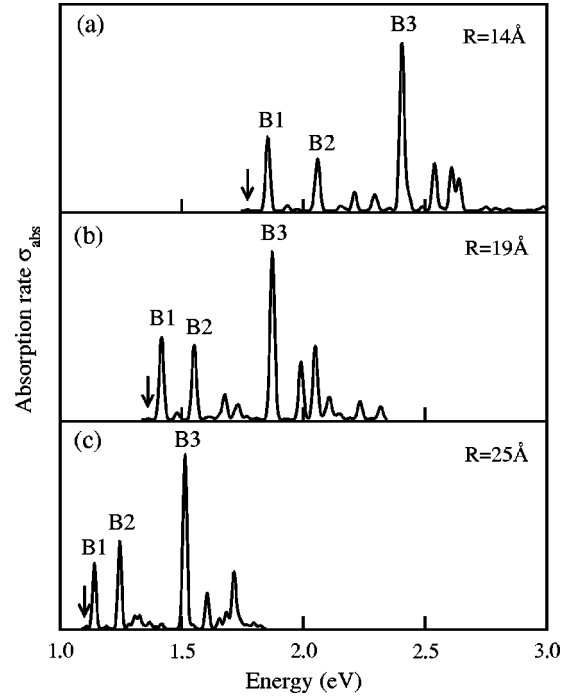


FIG. 3. Calculated exciton absorption spectra of InAs nanocrystals with radius (a) 14 Å, (b) 19 Å, and (c) 25 Å. The first three bright-exciton levels are identified by the three pronounced peaks B1, B2, and B3. The arrows indicate the lowest exciton levels which have weak oscillator strengths.

indicated by the arrows in Fig. 3 always shows a weak oscillator strength regardless of the nanocrystal radius. The first three bright-exciton levels labeled with B1, B2, and B3 are identified by the first three pronounced peaks of the absorption spectra in Fig. 3. Table III lists the electron and hole levels of D1, B1, B2, and B3 exciton levels.

To understand the origin of the oscillator strengths of low-lying exciton levels, we analyze the angular momenta of the electron and hole envelope functions of the exciton levels. The envelope function $c_{a;i\gamma\sigma}$ of a γ -basis orbital with spin σ is expanded in terms of spherical harmonics $Y_{lm}(\theta,\phi)$ to determine dominant angular momenta:

TABLE III. Electron and hole levels of the lowest exciton level and the first three bright-exciton levels, and the dominant angular momenta of the electron and hole envelope functions. The lowest exciton level (D1) is indicated by the arrow in absorption spectra shown in Fig. 3, while the first three bright-exciton levels (B1, B2, B3) are identified by the three pronounced absorption peaks. The n th lowest electron level and the n th lowest fourfold hole level are labeled as e_n and h_n , respectively. $c_{e;s}(c_{h;s})$ and $c_{e;p}(c_{h;p})$ denote the electron (hole) envelope function of the s and p orbitals, respectively.

Level	Composition	$c_{e;s}$	$c_{e;p}$	$c_{h;s}$	$c_{h;p}$
D1	$e_1 + h_1$	s -like	p -like	p -like	p -like
B1	$e_1 + h_2$	s -like	p -like	p -like	$(s+p)$ -like
B2	$e_1 + h_5$	s -like	p -like	p -like	$(s+p)$ -like
B3	$e_2 + h_1$	p -like	$(s+p)$ -like	p -like	p -like

TABLE IV. Compositions of electron and holes states in terms of orbital types. The calculated fraction of the electron and hole states in orbital type γ is the sum of the tight-binding coefficient squares $|c_{i\gamma\sigma}|^2$ over all atomic sites i and spins σ . The levels e_1 and e_2 are the first (twofold) and the second (sixfold) lowest electron levels of an InAs nanocrystal with radius 14 Å, respectively. Similarly, the levels h_1 and h_2 are the first (fourfold) and the second (fourfold) lowest hole levels.

Level	s orbital	p orbital	d orbital	s^* orbital
e_1	0.563	0.177	0.023	0.238
e_2	0.438	0.309	0.04	0.212
h_1	0.005	0.821	0.173	0.001
h_2	0.034	0.785	0.174	0.007

$$c_{a;i\gamma\sigma} \equiv c_{a;\gamma\sigma}(\mathbf{R}_i) = \sum_{\ell m} \alpha_{\ell m} Y_{\ell m}(\theta, \phi), \quad (23)$$

where the index a denotes e and h for electron and hole, respectively. The vector \mathbf{R}_i is a position vector of atom site i . The dominant angular momenta of the envelope functions of several low-lying exciton levels (D1, B1, B2, B3) are listed in Table III.

The compositions of electron and hole states in terms of orbital types determine which pair of electron and hole envelope functions contributes the most to the oscillator strengths. Table IV shows that the s and p orbitals are the dominant orbitals of electron and hole states, respectively. Moreover, the p orbitals are the most common orbitals of the electron and hole states. Therefore the principal part of the interorbital dipole moment is that between the s -orbital electron and the p -orbital hole envelope functions. Likewise, the principal part of the intraorbital dipole moment is that between the p -orbital electron and hole envelope functions. These two principal dipole moments contribute the most to the oscillator strengths.

The lowest exciton level is dim because the principal parts of the intra- and interorbital dipole moments do not satisfy the angular momentum selection rules given by Eqs. (11) and (12). The small oscillator strength of the lowest exciton level arises from (i) the intraorbital dipole moment between the s -like s -orbital electron and the p -like s -orbital hole envelope function, and (ii) the interorbital dipole moment between the p -like p -orbital electron and the p -like s -orbital hole envelope function. Typically, the oscillator strength of the lowest exciton level is smaller by two orders of magnitude than that of bright-exciton levels.

In bright exciton levels, their principal dipole moments satisfy the optical selection rule, yielding large oscillator strengths. For example, the B1 level is bright because (i) the p -like p -orbital electron and the s -like p -orbital hole envelope function yield a large intraorbital dipole moment, and (ii) the s -like s -orbital electron and s -like p -orbital hole lead to a large interorbital dipole moment. Typically, the intraorbital dipole moments are larger than the interorbital dipole moment by a factor of about 10 for nanocrystal radii R

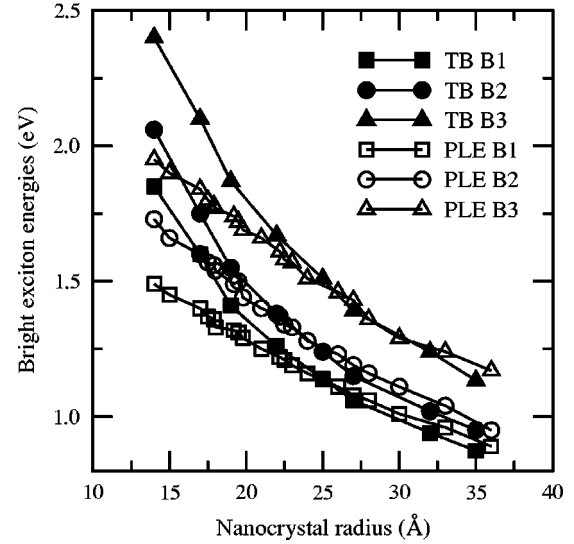


FIG. 4. Three lowest bright-exciton energies of InAs nanocrystals versus nanocrystal radius. The three lowest bright-exciton energies in the present tight-binding (TB) model are determined by the energies of the peaks B1, B2, and B3 defined in Fig. 3. Calculated exciton energies are compared with the energies of the first three strong photoluminescence peaks labeled as E_1 , E_3 , and E_5 in Ref. 26, respectively. The calculated energies agree better with the experimental energies as the nanocrystal size increases.

$=15\text{--}35$ Å considered in this work. Similar analyses can explain the origin of large oscillator strengths of other bright-exciton levels.

Due to the interplay between quantum confinement and spin-orbit coupling, the order of hole levels changes as a nanocrystal size changes. In small nanocrystals where level spacing Δ_{qc} due to quantum confinement is larger than spin-orbit splitting energy Δ_{so} , several two-fold hole levels appear in between fourfold hole levels. However, in large nanocrystals where Δ_{qc} is smaller than Δ_{so} , fewer twofold hole levels appear close to the band edges. In fact, for our biggest nanocrystal ($R=35$ Å) the first four lowest hole levels are each fourfold degenerate.

The exciton levels composed of the twofold hole levels near band edges and the lowest electron level are dark. In the exciton levels, the electron and hole envelope functions have the same total local angular momentum ($j=\frac{1}{2}$) and the same global angular momentum ($L=0$). Since the difference of the total angular momenta between the electron and hole level is zero, the exciton levels are optically forbidden. In higher hole levels, twofold hole levels with $L=1$ emerge and they form bright-exciton levels with the lowest electron level. These exciton levels correspond to small peaks between B2 and B3 in Fig. 3.

Figure 4 presents the nanocrystal size dependences of the three lowest bright-exciton energies identified in Fig. 3. The exciton energies are compared with those of PLE experiments.²⁶ The calculated energies agree better with the experimental energies as the nanocrystal radius increases. For small nanocrystals, the calculated energies scale as $R^{-0.8}$ with respect to nanocrystal radius R , while the experimental data scale as R^{-n} with $n \approx +0$. The flat curvature of the

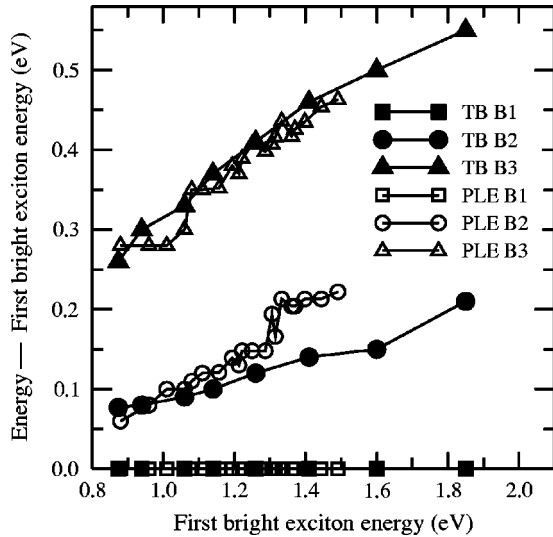


FIG. 5. First three bright-exciton energies relative to the lowest bright-exciton energy plotted with respect to the lowest bright-exciton energy. The first three exciton energies in the present tight-binding (TB) model are identified by the peaks B1, B2, and B3 in the absorption spectra shown in Fig. 3. The spacings of the identified three exciton energies are compared with the energy spacings of the first three strong photoluminescence peaks labeled as E_1 , E_3 , and E_5 in Ref. 26, respectively.

experimental energies is not explained by either the present tight-binding model or other empirical models.^{18,26}

Since precise experimental size determinations are difficult, it is more reliable to compare exciton energies relative to the lowest bright-exciton energy. Figure 5 presents B2 and B3 energies relative to B1 energies with respect to B1 energies. B3 energies agree well with corresponding experimental values, E_5 in Ref. 26, in a wide range of B1 energies. B2 energies agree less well with experimental values, E_3 in Ref. 26, in particular for large B1 energies which correspond to small nanocrystals. The experimental data for B2–B1 energies show discrete jump around the B1 energy of 1.3 eV, indicating a level crossing. This jump is not predicted by our calculations. The calculated B2 energies agree better with the experiment as a B1 energy decreases, that is, a nanocrystal size increases.

Figure 5 shows that the present model gives a better description of electron level spacings than hole level spacings. The energy difference between B1 and B2 is roughly the spacing between the second and fifth fourfold hole levels, while the difference between B1 and B3 is the spacing between the first and second electron levels. Since calculated energies B3–B1 agree with experimental values better than B2–B1, the electron level spacing is better described by our model than the hole. This can be explained by the difference between the characters of InAs conduction and valence bands. The lowest conduction band near the Γ point is almost isotropic and has no spin-orbit coupling. In contrast, the highest valence bands are complex due to the anisotropic effective masses of the heavy hole band, and the couplings among the heavy-hole, light-hole, and spin-split bands. Although the coupling between the conduction and valence

bands mixes band contributions to single-particle levels, the main parts of the electron and hole levels are from the conduction and valence bands, respectively. Hence the complexity of the valence-band structure makes it more difficult to obtain a good description for the hole levels than for the electron levels.

B. Electron and hole addition energies

One important physical value in the tunneling spectra is the spacing between the first conductance peaks of a positive and a negative bias-voltage side, which is labeled as E_{gap} in Fig. 1. This spacing is called a zero-current energy gap since a tunneling current is suppressed within a voltage region between these two peaks. In the present model, the zero-current energy gap is the sum of the first electron and hole addition energies:

$$E_{\text{gap}} \equiv \mu_1^e + \mu_1^h = E_1^e + E_1^h + \Sigma_1^{\text{pol},e} + \Sigma_1^{\text{pol},h} + W_1. \quad (24)$$

Therefore the zero-current energy gap differs from a single-particle energy gap by the sum of the electron and hole self-polarization energies and the electron-removal work function.

The effective dielectric constant ϵ_{out} of the nanocrystal environment and the closest distance d between the STM tip and the nanocrystal are estimated to calculate charging energies. The dielectric constant ϵ_{out} is determined by fitting $\Delta_{1,2}^e$ to the corresponding experimental value of an InAs nanocrystal with radius $R = 32 \text{ \AA}$. The best fit of $\Delta_{1,2}^e$ is obtained with $\epsilon_{\text{out}} = 4.5$. For d , we use the distance of the tip's closest approach to the nanocrystal, which is the length (about 5 \AA) of ligands surrounding the nanocrystal, since the accurate geometry of the STM setup is not available.²⁷ This approach provides the lower limit of the electron-removal work function.

Figure 6 presents the size dependences of the charging energies for zero-current energy gaps and that of the gaps with nanocrystal radii ranging from 15 to 35 \AA . Single-particle gaps contributing to the zero-current gaps range from 1.9 to 0.9 eV as the nanocrystal size increases, while total charging energies vary from 220 to 90 meV. Within the total charging energy, the electron and hole self-polarization energies are 80–40 meV each, and the work functions are 60–10 meV. The calculated zero-current gaps are compared with STM experimental gaps.^{27,37} As shown in Fig. 6(b), the calculated gaps agree well with the experiment for a full experimental range of InAs nanocrystal radii.

The electron and hole addition energies beyond the zero-current energy gap contain charge-carrier Coulomb energies and excited single-particle energies. The lowest electron level of spherical InAs nanocrystals is twofold, while the lowest hole level is fourfold. As a result, the first two tunneling electrons are assigned to the lowest electron level. Similarly, the first four tunneling holes are assigned to the lowest hole level. Therefore the spacing between the first two electron addition energies and those between the first four hole addition energies are determined solely by the charging energies. In contrast, the third electron and the fifth hole addition energies contain the energies of the second lowest

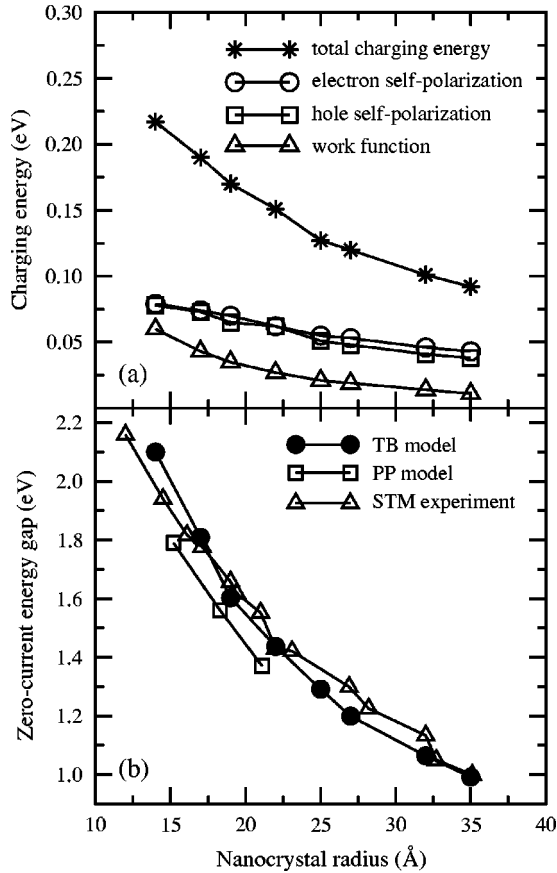


FIG. 6. (a) Calculated charging energies for zero-current energy gaps versus InAs nanocrystal radius R . (b) Zero-current energy gaps versus R . The size dependence of each component of the charging energy—electron and hole self-polarization energies and electron-removal work functions—is plotted. The zero-current gaps calculated with the present tight-binding (TB) model are plotted with respect to nanocrystal radius in comparison with those of pseudopotential (PP) calculations (Ref. 19) and STM experiments (Ref. 27). The present TB gaps are in good agreement with the experiment for a full range of nanocrystal radii ($R=10\text{--}40$ Å).

electron and hole levels in addition to charging energies, respectively. The third tunneling electron is assigned to the second lowest electron level since the lowest electron level is fully occupied by the first two tunneling electrons. Likewise, the fifth hole is assigned to the second lowest hole level. Consequently, the spacing between the second and third electron addition energies and that of the fourth and fifth hole addition energies are the sum of the level spacing and the charging energies. The spacings between these low-lying electron and hole addition energies are listed in Table V.

Calculated addition energy spacings of InAs nanocrystals with various radii are compared with those of STM experiments²⁷ in Fig. 7. The spacing $\Delta_{1,2}^e$ is in good agreement with the experiment. Note that only $\Delta_{1,2}^e$ with nanocrystal radius 32 Å is fitted to experiments to determine ϵ_{out} . The difference between calculated $\Delta_{2,3}^e$ and the experiment is less than 50 meV (10% error). The relatively good agreement for $\Delta_{2,3}^e$ shows that the second lowest electron level is well described by the $sp^3d^5s^*$ nearest-neighbor tight-binding model.

TABLE V. Addition energy spacings. The addition energy spacings are mainly determined by the Coulomb energy of one pair of charge carriers and a single-particle level spacing, since the variation of the self-polarization energies of different charge carriers and that of the Coulomb energies of a different pair of charge carriers are smaller than 10 meV. J^{ee} (J^{hh}) is the Coulomb energy of one pair of electrons (holes). $E_3^e - E_2^e$ ($E_5^h - E_4^h$) is the spacing between the first two lowest electron (hole) levels.

Electron	Hole
$\Delta_{1,2}^e \approx J^{\text{ee}}$	$\Delta_{1,2}^h = \Delta_{2,3}^h = \Delta_{3,4}^h \approx J^{\text{hh}} + W_1^h$
$\Delta_{2,3}^e \approx E_3^e - E_2^e + J^{\text{ee}}$	$\Delta_{4,5}^h \approx E_5^h - E_4^h + J^{\text{hh}} + W_1^h$

The spacing $\Delta_{1,2}^h$ is overestimated by 25 meV in the present model as shown in Fig. 7. The electron-removal work function may be the main cause of the small discrepancy in $\Delta_{1,2}^h$. The work function is modeled with a simplified description of the nanocrystal environment, which is illustrated in Fig. 2. Unlike other types of charging energies, the work function requires a good description of the electrostatic potential in a region between the nanocrystal and the STM tip as shown in Eq. (22). To improve the work function, an electrostatic potential of the inhomogeneous nanocrystal environment shown in Fig. 2 should be calculated.

Figure 7(b) shows that the present model underestimates the spacing $\Delta_{4,5}^h$ by about 100 meV. The charging energy of $\Delta_{4,5}^h$ is the same as $\Delta_{1,2}^h$, and the charging energy agrees with the experiment within an error of only a few tens of meV. Therefore the big discrepancy in $\Delta_{4,5}^h$ is attributed to the underestimation of the spacing between the two lowest hole levels.

IV. DISCUSSION

This work demonstrated the success of the tight-binding model for describing the many-body levels of optically excited and multiply charged nanocrystals. Specifically, calculated three lowest bright-exciton energies of InAs nanocrystals with radius larger than 20 Å show good agreement with PLE experiments within a 5% error. Calculated several low-lying electron and hole addition energies of InAs nanocrystals agree with STM experiments within a 10% error. These agreements show that the present model successfully describes both single-particle energies and many-body interaction energies. In particular, the good agreement for the exciton and addition energies involving excited single-particle energies shows that the tight-binding model accurately predicts not only the lowest electron and hole energies but also excited electron and hole energies.

In contrast to the success, the present tight-binding model does not agree well with experiments for (i) the bright exciton energies of InAs nanocrystals with radius smaller than 20 Å, and (ii) the fifth hole addition energies of InAs nanocrystals with all radii (10–40 Å) considered in this work. Calculated bright exciton energies for small InAs nanocrystals scale as $R^{-0.8}$ with respect to nanocrystal radius R , while experimental data scale as R^{-n} with $n \approx +0$. Hence the calculated exciton energies rapidly increase with increasing a

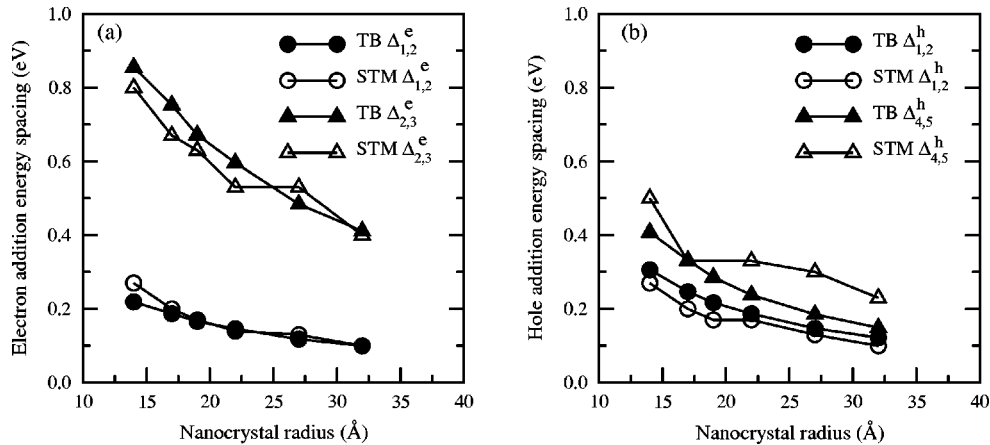


FIG. 7. (a) Electron addition energy spacings $\Delta_{1,2}^e$ and $\Delta_{2,3}^e$ versus nanocrystal radius R . (b) Hole addition energy spacings $\Delta_{1,2}^h$ and $\Delta_{4,5}^h$ versus R . The spacings are calculated with Eqs. (17) and (18) for R ranging from 15 to 35 Å. Corresponding STM experimental values taken from Ref. 27 are plotted for comparison. The spacing $\Delta_{1,2}^e$ at $R = 32$ Å is a fitted quantity to choose the effective dielectric constant of the nanocrystal environment $\epsilon_{\text{out}} = 4.5$.

nanocrystal radius, yielding bigger discrepancies with experimental energies. The present model underestimates the fifth hole addition energies by about 100 meV. Experimental uncertainties of size determinations³⁸ and bias-voltage drop distributions^{39,40} make it difficult to identify the main causes of the disagreements. Despite the difficulty, we focus on the possible causes of the disagreements resulting from the limits of the present model, and point out the ways to improve the model for future work. The discrepancies between our calculations and the experimental data can be explained by three possible reasons.

First, the effects of surface reconstruction and surface chemistry become important as a nanocrystal size decreases. The effects are excluded in the present model as we model the nanocrystal as a perfect zinc-blende structure with all dangling bonds at the surface terminated. Tight-binding studies for CdSe nanocrystals show that the inclusion of the surface reconstruction decreases the lowest bright-exciton energies by 100 meV for a nanocrystal with radius 12 Å.⁴¹ The decrease of the energies steadily decreases as the nanocrystal size increases.⁴¹ Moreover, recent first-principle calculations for Si nanoclusters show that imperfect surface passivation can reduce the gap by as much as 1.6 eV.¹⁵ The close agreement between the present model and STM experiment for the zero-current gap suggests that the lowest electron and hole states are insensitive to the surface reconstruction. In contrast, the several lowest bright exciton energies start to diverge for 20-Å-radius nanocrystals. The exciton energies involve excited hole energies. This suggests that the excited hole states are sensitive to the surface relaxation.

Second, the transferability of bulk tight-binding parameters to describe the single-particle Hamiltonian of nanocrystals is limited within the present model due to the deviation of a charge density in a nanocrystal from that in bulk. The present model uses bulk parameters, which are fitted to bulk band structures, without correcting them for nanocrystals with respect to the change of the local charge density. The density deviation from the bulk to the nanocrystal becomes larger as the ratio of surface to volume increases. Making the

parameters a functional of the charge density and achieving the self-consistency of the charge density and the parameters are a step forward to improve the transferability of the tight-binding model.⁴²

Third, the single-particle levels of charged nanocrystals with an electric field applied are different from those of uncharged nanocrystals in the absence of an electric field. The differences are neglected within the present model and other models.^{19,22} The charging and electric-field effects are expected to be larger on higher addition energies which involve more charge carriers and stronger electric fields. This expectation is consistent with the agreement between experiments and our calculations for several low-lying addition energies but the disagreement for the fifth hole addition energy. Self-consistent calculations of single-particle levels in the presence of excess charges and an applied electric field are needed to resolve the charging and the electric field effects on the single-particle levels.

The success of the tight-binding model in describing the many-body levels of relatively large chemically synthesized quantum dots suggests that the tight-binding model can quantitatively describe the optical and transport properties of larger quantum dots such as self-assembled and vertical dots. The present model for electron-hole interactions, electron-hole dipole moments, and charging energies, which are incorporated into the tight-binding model, can be easily extended to study the properties of the large dots. The suitability of the tight-binding model for describing small nanocrystals remains unresolved. Our results suggest that local effects, such as surface relaxation and the change of local charge densities, must be included more carefully as the nanocrystal size crosses from the mesoscopic scale to the molecular scale.

ACKNOWLEDGMENTS

We thank Joseph W. Lyding for helpful discussions. S.L. gladly acknowledges the hospitality of the UIUC NCSA during 2001–2002. This work was supported by the OSU, NSF

under Grant No. 9976550, and DOE–Basic Energy Sciences, Division of Materials Sciences (contract DE-FG02-99ER45795). Computational resources were provided by the National Center for Supercomputing Applications, the National Energy Research Scientific Computer Center, and the Ohio Supercomputer Center.

APPENDIX

Within the $sp^3d^5s^*$ nearest-neighbor tight-binding model including spin-orbit coupling, the effective single-particle Hamiltonian of InAs nanocrystals is

$$H_{\text{single}} = \sum_{i,\gamma,\sigma,\sigma'} u_{i\gamma\sigma\sigma'} |i\gamma\sigma\rangle \langle i\gamma\sigma'| + \sum_{\langle i,j \rangle, \gamma, \gamma', \sigma} t_{ij\gamma\gamma'}(\mathbf{R}_i - \mathbf{R}_j) |i\gamma\sigma\rangle \langle j\gamma'\sigma|. \quad (\text{A1})$$

The indices of the tight-binding basis orbital $|i\gamma\sigma\rangle$ are atomic-site i , orbital-type $\gamma = s, p^3, d^5, s^*$, and spin σ . The s^* orbital is an excited orbital with s symmetry. The closest link of the s^* orbital to a physical orbital would be an s orbital in the next shell. The main reason for including the s^*

orbital is to provide an additional degree of freedom in empirical fitting of tight-binding parameters. The Hamiltonian matrix elements, $u_{i\gamma\sigma\sigma'}$ and $t_{ij\gamma\gamma'}(\mathbf{R}_i - \mathbf{R}_j)$,⁴³ are parameterized for the InAs bulk band structure.²⁹ \mathbf{R}_i is the position vector of atom-site i . Only $t_{ij\gamma\gamma'}(\mathbf{R}_i - \mathbf{R}_j)$ between nearest neighbors $\langle i, j \rangle$ is included in the Hamiltonian. To mimic the effect of surface passivation by ligands, we adjust $u_{i\gamma\sigma\sigma'}$ of surface atoms by shifting the energies of sp^3 hybridized orbitals connected to ligands by 100 eV. This eliminates surface states lying in the middle of the single-particle gap.

For a nanocrystal composed of N_a atoms, the dimension of the Hamiltonian matrix is $2N_b N_a \times 2N_b N_a$, where N_b is the number of basis orbitals and is 10 for the $sp^3d^5s^*$ model. N_a ranges from 417 to 6395 as the nanocrystal radius increases from 14 to 35 Å. Selective *complex* eigenstates around the bulk band gap are obtained by the implicitly restarted arnoldi method using ARPACK.⁴⁴ For large nanocrystals, ARPACK and sparse-matrix-vector multiplications are parallelized using OpenMP.⁴⁵ The required total computation time and memory to obtain 40 eigenstates for a nanocrystal with radius 35 Å, the biggest computation in this work, are 88 h (88/60 h in real time) and 52 GB using 60 threads on SGI Origin2000 at NCSA, respectively.⁴⁶

-
- ¹L. Brus, Appl. Phys. A: Solids Surf. **53**, 465 (1991).
²M.A. Kastner, Phys. Today **46** (1), 24 (1993).
³A.P. Alivisatos, Science **271**, 933 (1996).
⁴*Quantum Dot Heterostructures* edited by D. Bimberg, M. Grundmann, and N. Ledentsov, (Wiley, Chichester, 1998).
⁵D.L. Klein, R. Roth, A.K.L. Lim, A.P. Alivisatos, and P.L. McEuen, Nature (London) **389**, 699 (1997).
⁶S. Tarucha, D.G. Austing, T. Honda, R.J. van der Hage, and L.P. Kouwenhoven, Phys. Rev. Lett. **77**, 3613 (1996).
⁷P.G. Eliseev, H. Li, A. Stintz, G.T. Liu, T.C. Newell, K.J. Malloy, and L.F. Lester, Appl. Phys. Lett. **77**, 262 (2000).
⁸H. Drexler, L. Leonard, W. Hansen, J.P. Kotthaus, and P.M. Petroff, Phys. Rev. Lett. **73**, 2252 (1994).
⁹T. Lundstrom, W. Schoenfeld, H. Lee, and P.M. Petroff, Science **286**, 2312 (1999).
¹⁰S. Kim, H. Mohseni, M. Erdtmann, E. Michel, C. Jelen, and M. Razeghi, Appl. Phys. Lett. **73**, 963 (1998).
¹¹P. Michler, A. Kiraz, C. Becher, W.V. Schoenfeld, P.M. Petroff, L. Zhang, E. Hu, and A. Lmamoglu, Science **290**, 2282 (2000).
¹²E. Biolatti, R.C. Iotti, P. Zanardi, and F. Rossi, Phys. Rev. Lett. **85**, 5647 (2000).
¹³F. Pederiva, C.J. Umrigar, and E. Lipparini, Phys. Rev. B **62**, 8120 (2000).
¹⁴S.O. Igor Vasiliev and J.R. Chelikowsky, Phys. Rev. Lett. **85**, 5647 (2000).
¹⁵A. Puzder, A.J. Williamson, J.C. Grossman, and G. Galli, Phys. Rev. Lett. **88**, 97401 (2002).
¹⁶A.L. Efros and M. Rosen, Annu. Rev. Mater. Sci. **30**, 475 (2000).
¹⁷R. Sakhel, L. Jönsson, and J.W. Wilkins, Phys. Rev. B **64**, 155322 (2001).
¹⁸A.J. Williamson and A. Zunger, Phys. Rev. B **61**, 1978 (2000).
¹⁹A. Franceschetti and A. Zunger, Phys. Rev. B **62**, 2614 (2000).
²⁰K. Leung and K.B. Whaley, Phys. Rev. B **56**, 7455 (1997).
²¹G. Allan, Y.M. Niquet, and C. Delerue, Appl. Phys. Lett. **77**, 639 (2000).
²²Y.M. Niquet, C. Delerue, M. Lannoo, and G. Allan, Phys. Rev. B **64**, 113305 (2001).
²³S. Lee, L. Jönsson, J.W. Wilkins, G.W. Bryant, and G. Klimeck, Phys. Rev. B **63**, 195318 (2001).
²⁴S. Fafard, M. Spanner, J.P. McCaffrey, and Z.R. Wasilewski, Appl. Phys. Lett. **76**, 2268 (2000).
²⁵C.B. Murray, D.J. Norris, and M.G. Bawendi, J. Am. Chem. Soc. **115**, 8706 (1993).
²⁶U. Banin, C.J. Lee, A.A. Guzelian, A.V. Kadavanich, A.P. Alivisatos, W. Jaskolski, G.W. Bryant, A.L. Efros, and M. Rosen, J. Chem. Phys. **109**, 2306 (1998).
²⁷U. Banin, Y. Cao, D. Katz, and O. Millo, Nature (London) **400**, 542 (1999).
²⁸A. Franceschetti and A. Zunger, Appl. Phys. Lett. **76**, 1731 (2000).
²⁹J.-M. Jancu, R. Scholz, F. Beltram, and F. Bassani, Phys. Rev. B **57**, 6493 (1998).
³⁰D. Helmholz, L.C.L.Y. Voon, and W. Ge, Phys. Status Solidi B **231**, 457 (2002).
³¹The energy of the hole level is the negative of the corresponding single-particle level. The hole wave function is the conjugate of the single-particle wave function, following the second quantization model in which a hole state is a state resulting from an annihilation operator applied to an occupied single-particle level. In addition, the spin of hole state is the opposite of that of the single-particle level.

- ³²R. Resta, Phys. Rev. B **16**, 2717 (1977).
- ³³D.R. Penn, Phys. Rev. **128**, 2093 (1962).
- ³⁴R. Tsu, L. Ioriatti, J. Harvey, H. Shen, and R. Lux, in *Microcrystalline Semiconductors: Materials Science and Devices*, edited by P. M. Fauchet, C. C. Tsai, L. T. Canham, I. Shimizu, and Y. Aoyagi, Mater. Res. Soc. Symp. Proc. No. **283** (Materials Research Society, Pittsburgh, 1993).
- ³⁵W. H. Press, S. A. Teukolsky, W. T. Vetterling, and B. P. Flannery, *Numerical Recipes in C: The Art of Scientific Computing* (Cambridge University Press, Cambridge, England, 1999), 2nd ed.
- ³⁶L. Banyai, P. Gilliot, Y.Z. Hu, and S.W. Koch, Phys. Rev. B **45**, 14 136 (1992).
- ³⁷In the STM experiment, the STM tips are retracted from the nanocrystal far enough to make most of the bias voltage drop across a tip-nanocrystal junction (J1) (Ref. 27). Therefore we approximate the voltage drop across J1 with the total bias voltage, that is the upper limit of the voltage drop across J1.
- ³⁸In the PLE experiment, its size measurement with transmission electron microscopy (TEM) may underestimate a nanocrystal radius by approximately 2.5 Å, because TEM is insensitive to a nonperiodic layer near the nanocrystal surface (Ref. 26). In the STM experiment, STM topographic images may overestimate a nanocrystal size due to the tip-nanocrystal convolution effect (Ref. 27).
- ³⁹D. Katz, O. Millo, S.-H. Kan, and U. Banin, Appl. Phys. Lett. **79**, 117 (2001).
- ⁴⁰Katz, *et al.* (Ref. 39) estimate that the ratio of the voltage drop across J1 to that across J2 is approximately 10 (see the inset of Fig. 1 for the definitions of J1 and J2). This estimation is based on theoretical tunneling simulations combined with pseudopotential calculations (Ref. 18) for single-particle levels, but not based on experimental measurements of, for instance, the capacitances and resistances of J1 and J2. Therefore approximating the voltage drop across J1 with the total bias voltage has a few tens of percent of uncertainties.
- ⁴¹K. Leung and K.B. Whaley, J. Chem. Phys. **110**, 11 012 (1999).
- ⁴²F. Liu, Phys. Rev. B **52**, 10 677 (1995).
- ⁴³J.C. Slater, Phys. Rev. **36**, 57 (1930).
- ⁴⁴[Http://www.caam.rice.edu/software/ARPACK/](http://www.caam.rice.edu/software/ARPACK/). Use of this software does not constitute an endorsement or certification by NIST.
- ⁴⁵[Http://www.physics.ohio-state.edu/ohmms/](http://www.physics.ohio-state.edu/ohmms/). Use of this software does not constitute an endorsement or certification by NIST.
- ⁴⁶Use of this product does not constitute an endorsement or certification by NIST.